Supplementary Information

The Role of Solid-Melt Interfaces in Self-Catalyzed Growth Kinetics of III-Nitride Semiconductors

Zhucong Xi[1,+], Abby Liu[1,+], Xiaobo Chen[2], Catherine Huang[1], Meng Li[2], Dmitri N. Zakharov[2], Judith C. Yang[2,3,4], Rachel S. Goldman[1,5,6], and Liang Qi[1,*]

[1]Department of Materials Science and Engineering, University of Michigan, Ann Arbor, MI 48109, USA
[2]Center for Functional Nanomaterials, Brookhaven National Laboratory, Upton, NY 11973, USA
[3]Department of Chemical and Petroleum Engineering, University of Pittsburgh, Pittsburgh, PA 15261, USA
[4]Department of Physics and Astronomy, University of Pittsburgh, Pittsburgh, PA 15261, USA
[5]Department of Physics, University of Michigan, Ann Arbor, MI 48109, USA
[6]Applied Physics Program, University of Michigan, Ann Arbor, MI 48109, USA
[*]qiliang@umich.edu
[+]these authors contributed equally to this work

Supplementary Note S1: Ab initio molecular dynamics simulations of the interface

To characterize the atomic structure and interface-induced layering at the Ga–GaN solid–liquid interface and to verify the accuracy of the machine learning interatomic potentialss (MLIPs) used in this work, we performed *ab initio* molecular dynamics (AIMD) simulations. The simulation cell, as shown in Fig. S1, was constructed along the Ga-polar wurtzite (WZ)(0001) direction and consisted of a GaN slab in contact with a liquid Ga region. The crystalline substrate was modeled using a slab containing six Ga-N bilayers with in-plane dimensions of 2×4 GaN unit cells, corresponding to 96 N and 96 Ga atoms in total. A liquid Ga region containing an additional 128 Ga atoms was placed above the surface to form the solid-melt interface. During the simulation, the bottom Ga-N bilayer was fixed, and a vacuum region of 15 Å was introduced above the liquid region to avoid spurious interactions between periodic images along the surface-normal direction.

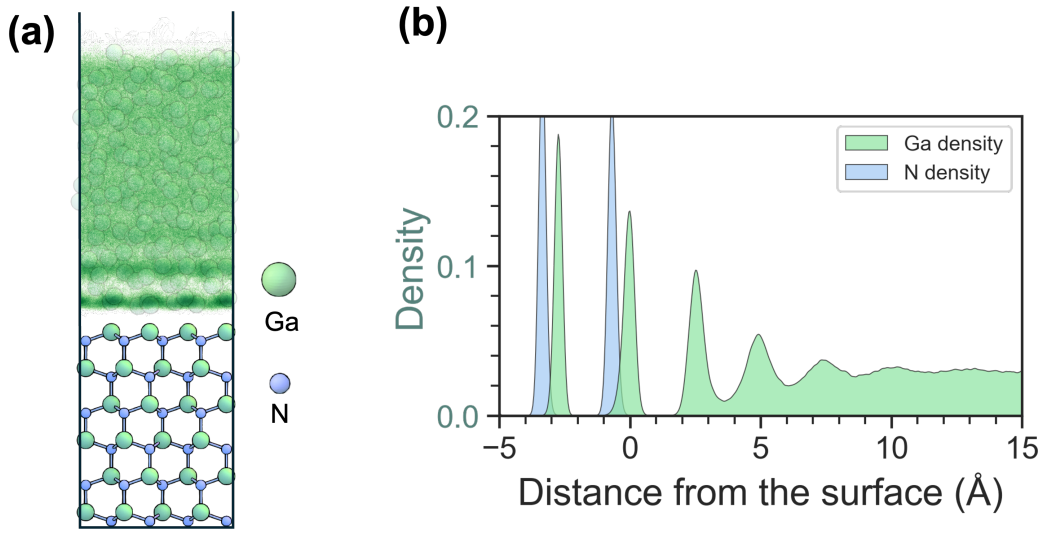

Figure S1. Ab initio molecular dynamics simulations at GaN(*s*)-Ga(*l*) Ga-polar interface. (a): Slab model of the Ga-polar WZ(0001) interface used for AIMD calculations. Ga and N atoms are depicted in green and blue-gray, respectively. The liquid side is visualized by Ga atomic number density, superimposed on the atomistic structures. **(b)**: Time-averaged atomic number density profiles of Ga (green) and N (blue-gray) as a function of distance from the surface.

The AIMD calculations were carried out using Vienna *Ab Initio* Simulation Package (VASP)[1,2] with the Perdew-Burke-Ernzerhof (PBE) exchange-correlation functional[3] and projector-augmented wave potentials (PAW) pseudopotentials[4]. Ga pseudopotentials without explicit *d* electrons were employed. The electronic self-consistency loop was converged to 10^{-4} eV in each step, using a plane-wave cutoff energy of 550.0 eV and Gaussian smearing of 0.05 eV. Owing to the large size of the simulation cell, a Γ-point-only k-point grid was used. The simulations were performed with a time step of 1 fs for a total duration of 10 ps.

Supplementary Note S2: Migration barriers on GaN pristine surface

WZ(0001) surface via different simulation methods. These results establish the reference for interfacial kinetics in the absence of liquid Ga and are used in the main text to highlight the catalytic effect of liquid Ga. The slab, as shown in Fig. S2, contained four Ga-N bilayers separated by a 12 Å vacuum, with a single N adatom embedded on the surface.The bottom surface was H-passivated to remove artificial dangling-bond effects. In-plane supercells of 2×4 units were used, corresponding to 16 N and 16 Ga atoms per bilayer.

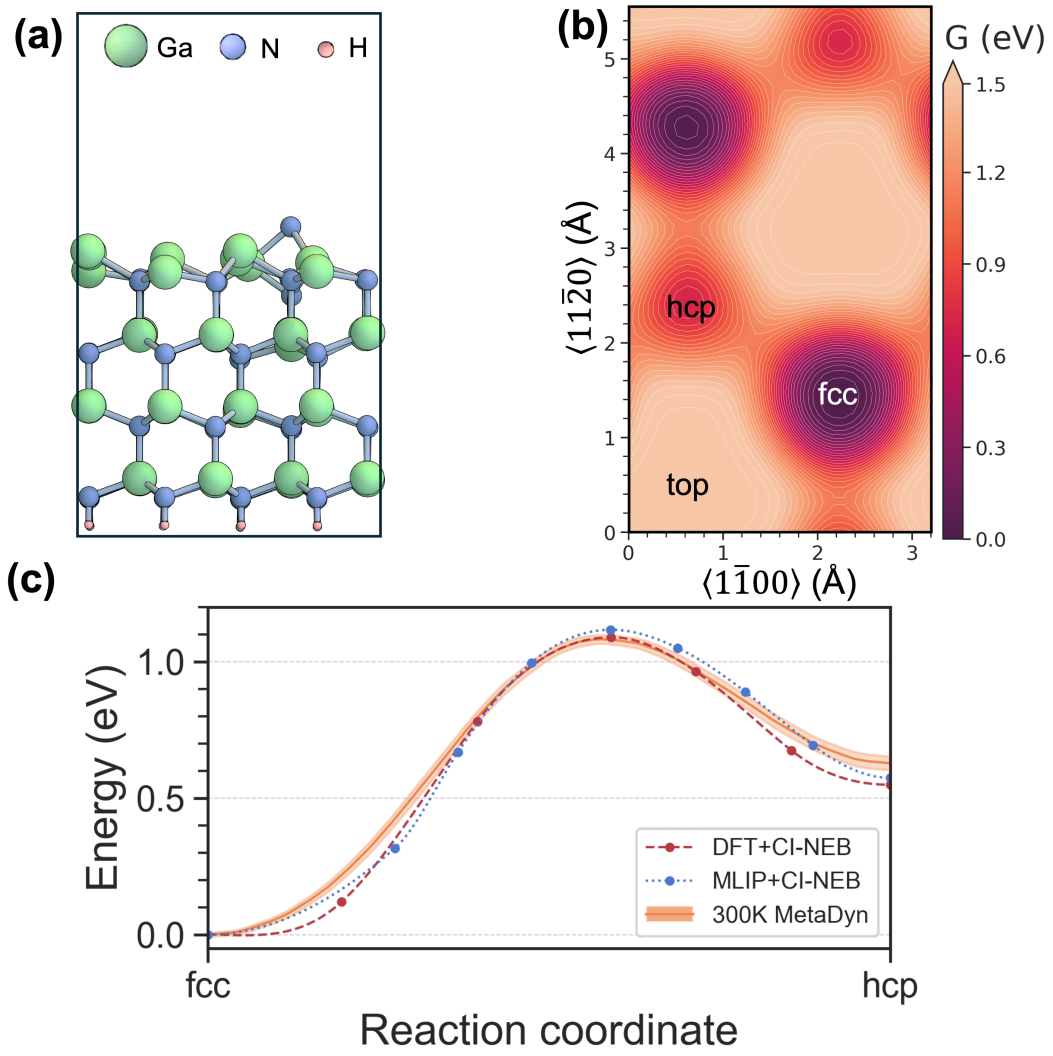

Figure S2. Migration barriers for an N adatom at GaN pristine Ga-polar surface. **(a)**: Slab model of the pristine Ga-polar WZ(0001) surface used for calculations; the back side is H-passivated (Ga: green, N: blue-gray, H: pink). **(b)**: Two-dimensional free-energy surface $G(x,y)$ at 300 K from well-tempered metadynamics for an N adatom restrained to the surface. Minima occur with threefold rotational symmetry at fcc and hcp sites. Axes are along $\langle 1\bar{1}00 \rangle$ and $\langle 11\bar{2}0 \rangle$. **(c)**: Minimum-energy path between hollow sites showing excellent agreement among DFT+CI-NEB (red dashed), MLIP+CI-NEB (blue dotted), and 300 K metadynamics (orange band, mean $\pm$ standard error). All methods yield a pristine-surface migration barrier of $\sim$1.1 eV, much larger than the barriers at the solid-melt interfaces reported in the main text.

Density functional theory (DFT) calculations, conducted by VASP[1,2] and the Transition States Tools (VTST) package[5,6], employed the PBE exchange-correlation functional[3] with PAW pseudopotentials[4]. Ga pseudopotentials treating the *d* electrons explicitly as valence states were employed. The bottom of the slab was passivated with pseudo-H atoms, which have fractional valence electrons. The total energies for supercells of the initial and final states were converged to 10^{-6} eV/cell for the ionic relaxation loop and 10^{-7} eV for the electronic self-consistency loop, using a plane-wave cutoff energy of 550.0 eV and Gaussian smearing of 0.05 eV. A $3 \times 3 \times 1$ Γ-centered k-point grid was applied for the supercell, with a k-point spacing value

of approximately ~ 0.20 Å^{-1}. Five intermediate images were linearly interpolated between the relaxed initial and final states. The artificial spring constant was set to 5 eV/Å^2.

MLIP-based climbing image nudged elastic band (CI-NEB) and metadynamics calculations used a larger $4 \times 8 \times 8$ slab. Initial structures from the MLIP were converged using a Conjugate Gradient algorithm with Large-scale Atomic/Molecular Massively Parallel Simulator (LAMMPS)[7,8]. Seven middle images were linearly interpolated for CI-NEB. Free-energy barriers at finite temperatures were obtained from well-tempered metadynamics using PLUMED[9,10] plus LAMMPS. The simulation temperature was set to 300 K with a Langevin thermostat (0.1 ps damping). We used the same two-dimensional CVs as in the interface lateral-migration calculations: the in-plane coordinates (x,y) of the N adatom, defined by projections onto the two surface lattice vectors. Periodic boundary conditions were applied in CV space so that (x,y) was mapped to the first unit cell during bias deposition and reweighting, enabling more efficient sampling of symmetry-equivalent minima. Well-tempered metadynamics parameters matched the main-text setup: initial hill height of 0.01 eV, Gaussian widths of 0.20 Å, a bias factor of 5, a hill stride of 0.4 ps, and a total biasing time of 10 ns.

All three approaches yield mutually consistent pristine-surface migration kinetics. On Ga-polar WZ-GaN(0001), the migration barrier is ~ 1.1 eV along the pathway from the fcc sites to the hcp sites. This agrees with prior reports[11]. These pristine-surface barriers are $\sim$2-3 times larger than the liquid-covered interface migration free energies (0.56 eV), quantitatively supporting the Ga catalytic effects advanced in the main text.

Supplementary Note S3: N pair-interaction at the interfaces

To quantify the effective interaction between two N adatoms at the GaN(s)-Ga(l) interface, we computed one-dimensional free energy using well-tempered metadynamics with the same PreFerred Potential (PFP), $T = 1000$ K, 1 fs timestep, and a Langevin thermostat (0.1 ps damping) as in the main-text simulations. Ga-polar WZ(0001) and N-polar WZ$(000\bar{1})$ slabs (768-atom GaN plus a 500-atom Ga melt) were employed. Two N adatoms were then introduced at the solid-melt interface. The systems were pre-equilibrated for 5 ps. The collective variable (CV) was the in-plane distance separation distance of two N adatoms, biased with Gaussian hills (initial height 0.01 eV, width 0.10 Å, stride 0.4 ps, bias factor 5) for 10 ns. To isolate lateral interactions, each N was softly restrained along z to the first adsorption well of its respective polarity, which was identified from the single-adatom vertical free energy, to prevent drift into the bulk liquid or desorption.

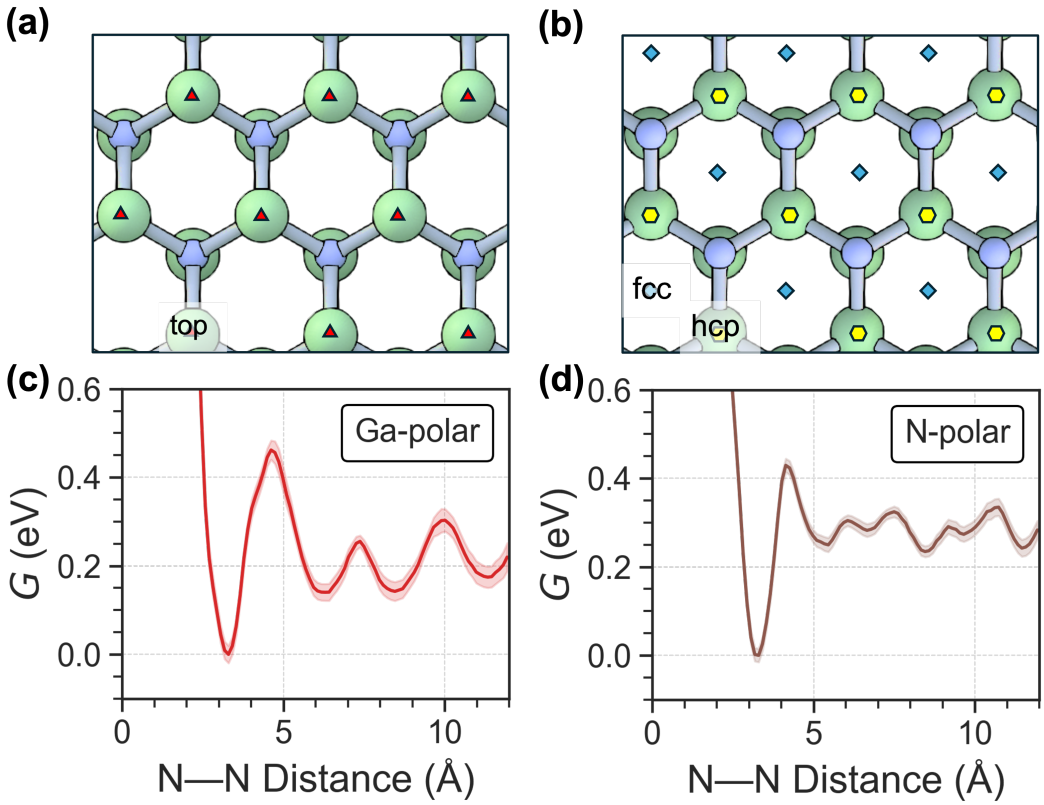

Figure S3. Pair-interaction free energies of N adatoms at GaN(s)-Ga(l) interfaces. (a)-(b): Top views of the Ga-polar (**a**) and N-polar (**b**) terraces showing the preferred adsorption sites for reference N adatoms (Ga-polar: top; N-polar: fcc/hcp). **(c)-(d)**: Interaction free energy G between two N adatoms as a function of their in-plane separation distance, obtained by well-tempered metadynamics at $T = 1000$ K. Both terminations exhibit strong short-range repulsion and weak oscillatory coupling at larger separations. Shaded bands indicate mean $\pm$ standard error from block-averaged reweighting.

Fig. S3 summarizes the two-adatom metadynamics used to describe the interactions between N adatoms at the interface. Figs. S3a and b show atomistic snapshots of preferred adsorption sites for the Ga-polar WZ(0001) and N-polar WZ$(000\bar{1})$ interfaces, respectively. The sites are identified from the single-adatom lateral migration free-energy landscapes (FELs). As presented in Figs. S3c and d. In both cases, the FELs, G, exhibits a steep short-range repulsion that forbids co-occupation of the same site, a pronounced minimum at $\sim$3.2 Å, corresponding to the first nearest neighbor distance, and damped oscillations at larger distances arising from the periodic spacing of adsorption sites. In both cases, the free-energy profile shows a difference of about $\sim$0.2 eV, corresponding to the bonding energy between two N adatoms at the interface, denoted as $E_b^{\text{N-N}}$. This value was then used in the bond-counting model to estimate the driving force for N migration, expressed as

$$\Delta E = \Delta n \cdot E_b^{\text{N-N}} \tag{S1}$$

Here, Δn is the number of first-nearest N-N bond changes before and after the N adatom hop at the interface. This formulation directly links the change in bond count to the corresponding migration driving force. Thus, the bond-counting model provides a simple yet quantitative way to capture how N-N bonding influences migration.

Supplementary Note S4: Effects of interface-induced atomic layering and charge redistribution on N adsorption free-energy landscapes at interfaces

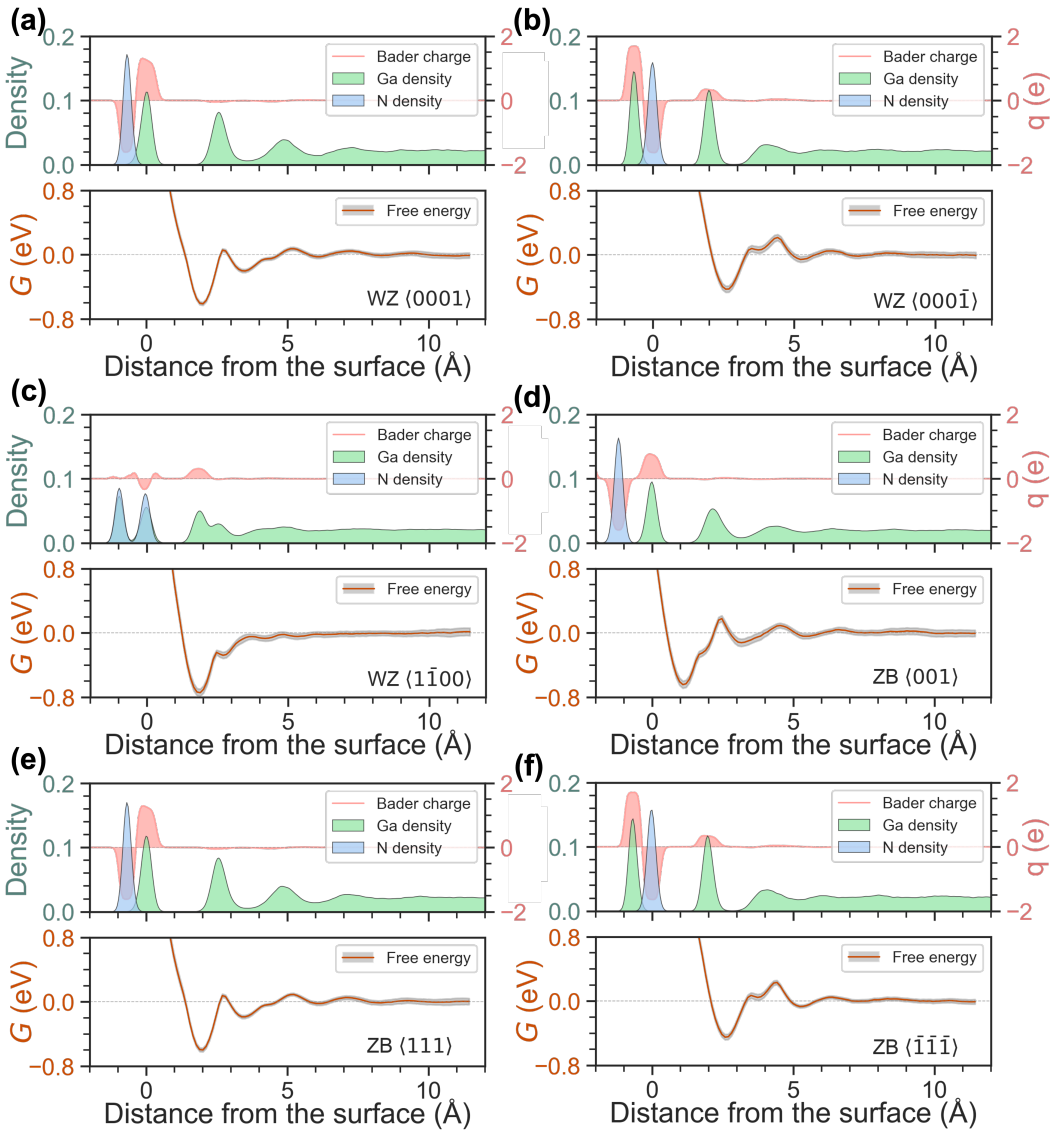

Figure S4. Coupling between interfacial layering, Bader charge distribution, and N adatom adsorption free-energy landscapes at GaN(*s*)-Ga(*l*) interfaces. (a)-(f): For each interface orientation and polarity, the upper panel shows time-averaged atomic number density profiles of Ga (green) and N (blue-gray) along the surface-normal direction (left axis), overlaid with the planar-averaged Bader charge distribution $q(z)$ (red, right axis). The lower panel shows the corresponding one-dimensional adsorption free-energy profile $G(z)$ for an incoming N adatom, obtained from well-tempered metadynamics. Results are shown for representative facets: WZ$\langle 0001\rangle$ (**a**), WZ$\langle 000\bar{1}\rangle$ (**b**), WZ$\langle 1\bar{1}00\rangle$ (**c**), ZB$\langle 001\rangle$ (**d**), ZB$\langle 111\rangle$ (**e**), and ZB$\langle \bar{1}\bar{1}\bar{1}\rangle$ (**f**).

Fig. S4 summarizes how interfacial liquid ordering and electronic redistribution jointly shape the adsorption FEL of N adatoms at GaN(*s*)-Ga(*l*) interfaces. Representative facets of both WZand zinc blende (ZB) interfaces are shown, including polar and non-polar orientations. For each interface, the upper panel displays the time-averaged atomic number density profiles of Ga and N along the surface-normal direction, together with the planar-averaged Bader charge distribution. The lower panel presents the corresponding one-dimensional adsorption free-energy profile for an incoming N adatom, obtained from well-tempered metadynamics.

Supplementary Note S5: Derivation for the steady-state equation

We treat the interfacial incorporation of N as diffusion driven by the concentration gradient and the free energy gradient. The total N flux in the direction perpendicular to the growth plane is given: To derive the steady-state solution for the N adatom flux, J, we begin with the master equation, which is a modified form of Fick's first law incorporating a chemical potential gradient:

$$J_{\mathrm{N}} = -D\frac{dc(z)}{dz} - \frac{Dc(z)}{k_B T}\frac{dG(z)}{dz} \tag{S2}$$

where D is the diffusivity, $c(z)$ is the concentration, $G(z)$ is the chemical potential (free energy), k_B is the Boltzmann constant, and T is the temperature. Under steady-state conditions, the flux J_{N} is constant. We can rearrange this first-order linear ordinary differential equation into the standard form:

$$\frac{dc(z)}{dz} + \frac{c(z)}{k_B T}\frac{dG(z)}{dz} = -\frac{J_{\mathrm{N}}}{D} \tag{S3}$$

This equation can be solved using an integrating factor $\exp\left(\frac{G(z)}{k_B T}\right)$:

$$\exp\left(\frac{G(z)}{k_B T}\right)\frac{dc}{dz} + \exp\left(\frac{G(z)}{k_B T}\right)\frac{c(z)}{k_B T}\frac{dG}{dz} = -\frac{J_{\mathrm{N}}}{D}\exp\left(\frac{G(z)}{k_B T}\right) \tag{S4}$$

Thus, our equation becomes:

$$\frac{d}{dz}\left(c(z)\exp\left(\frac{G(z)}{k_B T}\right)\right) = -\frac{J_{\mathrm{N}}}{D}\exp\left(\frac{G(z)}{k_B T}\right) \tag{S5}$$

We now integrate both sides with respect to z from the interface at $z = z_{\mathrm{ads}}$ to a position $z = z_{\mathrm{bulk}}$ far into the liquid:

$$\int_{z_{\mathrm{ads}}}^{z_{\mathrm{bulk}}} \frac{d}{dz}\left(c(z)\exp\left(\frac{G(z)}{k_B T}\right)\right) dz = -\frac{J_{\mathrm{N}}}{D}\int_{z_{\mathrm{ads}}}^{z_{\mathrm{bulk}}} \exp\left(\frac{G(z)}{k_B T}\right) dz \tag{S6}$$

Finally, applying the fundamental theorem of calculus and rearranging the terms in the numerator gives the expression for the steady-state flux as:

$$J_{\mathrm{N}} = D\left(\frac{c(z_{\mathrm{ads}})\exp\left(\frac{G(z_{\mathrm{ads}})}{k_B T}\right) - c(z_{\mathrm{bulk}})\exp\left(\frac{G(z_{\mathrm{bulk}})}{k_B T}\right)}{\int_{z_{\mathrm{ads}}}^{z_{\mathrm{bulk}}} \exp\left(\frac{G(z)}{k_B T}\right) dz}\right) \tag{S7}$$

The sign convention takes $+z$ from solid to liquid; thus, a negative J_{N} corresponds to net flux from liquid toward the solid (growth).

Supplementary Note S6: Diffusivity of N in liquid Ga

We determined the tracer diffusivity of N in liquid Ga, from equilibrium molecular dynamics (MD) using the same MLIP. To do so, we simulated 800 Ga atoms in liquid plus a single N probe atom in a cubic periodic cell at sampled temperatures of 900, 1000, 1100, and 1200 K. The system was equilibrated for 20 ps in the isothermal-isobaric (NPT) ensemble using the Nosé-Hoover barostat with damping of 1 ps and the Langevin thermostat with damping of 0.1 ps. After equilibration, both the thermostat and the barostat were removed, and the simulation was run in the microcanonical (NVE) ensemble for 200 ps.

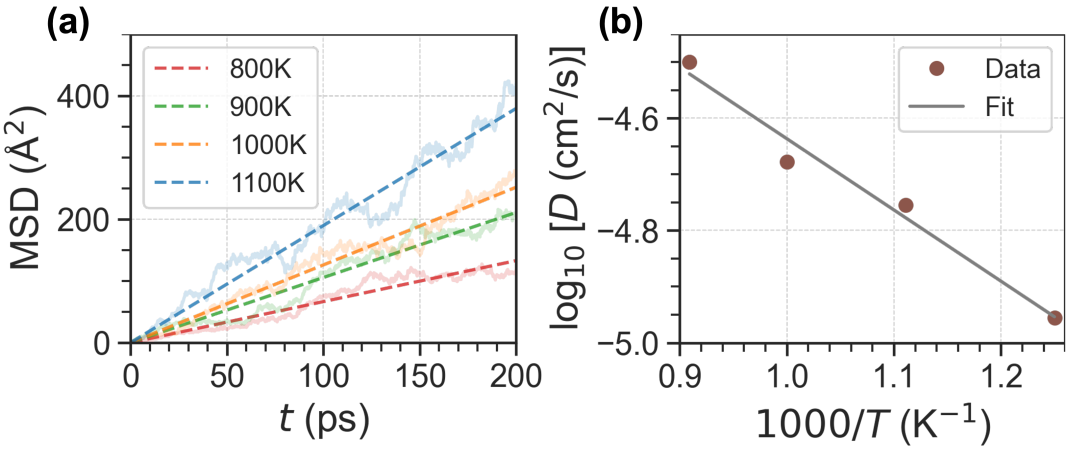

Figure S5. Diffusivity of N in liquid Ga. (a): Mean-squared displacement (MSD) of a single N probe in molten Ga at 800-1100K (solid curves). Dashed lines are linear fits in the diffusive regime used with the Einstein relation. **(b)**: Arrhenius representation of the diffusivity, $\log_{10} D$ ($\mathrm{cm^2 s^{-1}}$) versus $1000/T$; points are MD values and the solid line is the best linear fit, whose slope yields the activation energy and the intercept shows the prefactor. The resulting $D(T)$ is used in the diffusion-limited growth model.

During the simulation, we measured the mean-squared displacement (MSD) of the N probe:

$$\langle [\Delta R(t)]^2 \rangle = \frac{1}{n_{\mathrm{probe}}} \sum_{i=1}^{n_{\mathrm{probe}}} [\boldsymbol{R}_i(t) - \boldsymbol{R}_i(0)]^2 . \tag{S8}$$

Here, n_{probe} is the number of probe atoms, which equals 1 in our setup. $\boldsymbol{R}_i(i)$ is the position of atom i at t time. The MSD was accumulated along each temperature, as shown in Fig. S5a. The diffusivity of N was obtained from the Einstein relation for three-dimensional diffusion,

$$D = \frac{1}{6} \frac{d}{dt} \langle [\Delta R(t)]^2 \rangle, \tag{S9}$$

where D was computed by first making a linear approximation to the MSD, as shown in the dashed line Fig. S5a.

An Arrhenius analysis was performed by fitting the diffusivity as a function of temperature, $D(T)$:

$$D(T) = D_0 \exp\left(-\frac{E_D}{k_B T} \right). \tag{S10}$$

This is equivalently a linear regression of $\log D$ versus $1/T$, as shown in Fig. S5b. Points in Fig. S5b are the values obtained from the MD simulations, and the solid line is the least squares linear fit. The slope yields the activation energy E_D and the intercept gives the prefactor D_0. The resulting temperature-dependent diffusivity $D(T)$ is used directly in the diffusion-limited growth model in the main text.

Supplementary Note S7: Solubility of N in liquid Ga

We quantified the equilibrium solubility of N in liquid Ga through a two-step free energy calculation evaluated by well-tempered metadynamics at 1000 K using the MLIP described in the main text. The conceptual illustration of this two-step method is shown in Fig. S6a. The first step is the transfer of an N_2 molecule from the gas phase into the Ga melt, and the second step is dissociation of the solvated N_2 molecule.

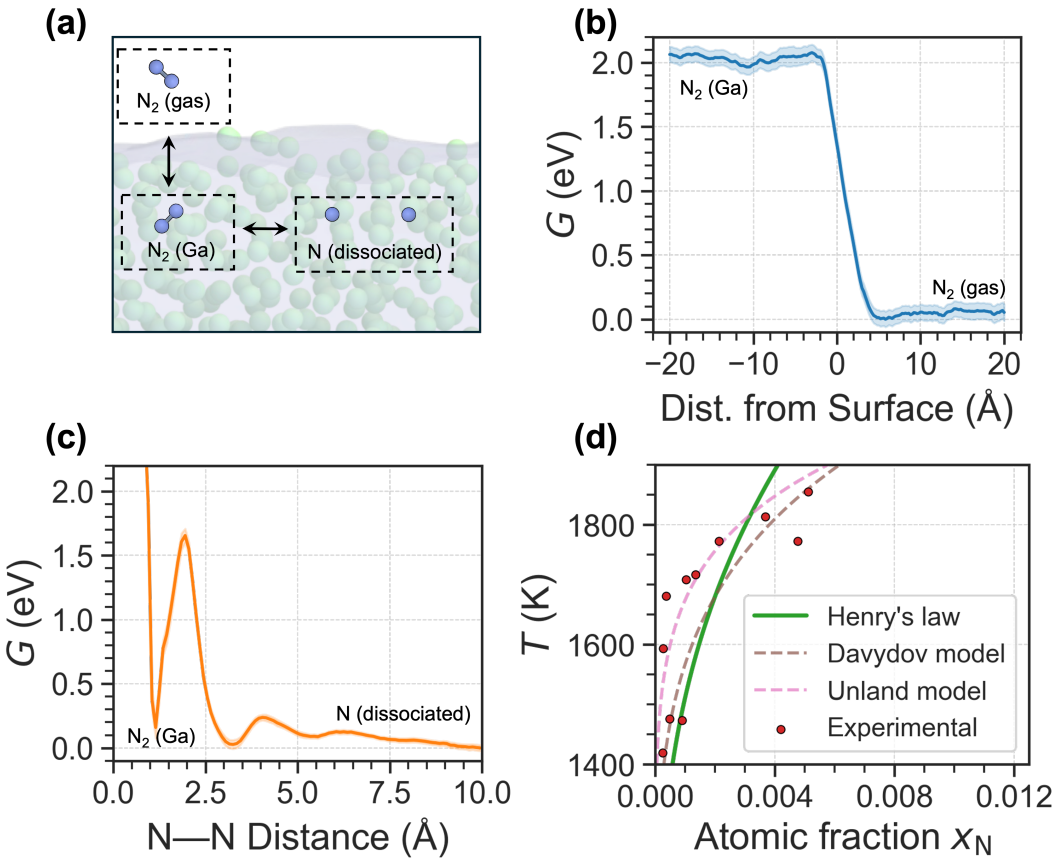

Figure S6. Solubility of N in Ga liquid from metadynamics simulations. **(a)**: Conceptual illustration of N_2 solvation with an N_2 molecule in the gas phase, an N_2 molecule solvated in Ga, and two dissociated N atoms in the Ga liquid. **(b)**: Solvation free-energy profile $G(z)$ at 1000 K as a function of the distance of N_2 from the liquid surface, showing a ∼2 eV to transfer N_2 into Ga. **(c)**: Free-energy profile for N_2 dissociation in Ga versus N-N separation distance, with a ∼1.7 eV barrier and an dissociation energy of ∼0.15 eV per N pair. **(d)**: Predicted N atomic fraction x_N as a function of temperature using the Henry's law expression derived from our free energy (green), compared with two empirical CALPHAD models (Davydov[12,13] and Unland[14]; dashed) and representative experimental points (red circles)[15–19]. All approaches indicate extremely low N solubility in Ga.

For the first step:

$$N_2(\text{gas}) \leftrightarrow N_2(\text{Ga liquid}), \tag{S11}$$

the solvation free energy $\Delta G_{\text{solv}}^{N_2}$ was computed with a CV defined as the distance between the center of mass of the Ga liquid slab and that of N_2. The simulation cell contained 800 Ga atoms and one N_2 molecule. A Lennard-Jones wall at the bottom of the slab stabilized the liquid and prevented drift. The system was pre-equilibrated for 10 ps with a Langevin thermostat (0.1 ps damping). Gaussian hills of width 0.30 Å and initial height 0.3 eV were deposited every 0.4 ps with a bias factor of 20 for a total of 10 ns. The resulting profile, as shown in Fig. S6b, shows a ∼ 2.0 eV penalty per molecule to transfer N_2 into the liquid, indicating very unfavorable solvation at these conditions.

For the second step:

$$N_2(\text{Ga liquid}) \leftrightarrow 2N(\text{Ga liquid}), \tag{S12}$$

the dissociation free energy, $\Delta G^{N_2}_{diss}$, was evaluated in a fully periodic box containing 800 Ga atoms and one N_2. After 10 ps equilibration at 1000 K using a Langevin thermostat and Nosé-Hoover barostat, we biased the N-N bond length as the CV. Gaussian width was 0.10 Å, initial height 0.04 eV, bias factor 10, and hills were deposited every 0.4 ps for 10 ns. The free-energy profile, as shown in Fig. S6c, exhibits a dissociation barrier of ∼1.6-1.7 eV and a dissociation free energy of ∼0.15 eV per molecule at 1000 K.

Combining the two steps yields the standard free energy for producing dissolved atomic N from gas-phase N_2:

$$\frac{1}{2}\mathrm{N_2(gas)} \leftrightarrow \mathrm{N(Ga\ liquid)}, \tag{S13}$$

with the reaction energy $\Delta G^{N}_{solv}(T) = \frac{1}{2}\left(\Delta G^{N_2}_{solv}(T) + \Delta G^{N_2}_{diss}(T)\right) \approx 0.85$ eV/atom at 1000 K. At equilibrium, it requires

$$\frac{1}{2}\mu^{gas}_{N_2}(T, p_{N_2}) = \mu^{liquid}_{N}(T, x_N) \tag{S14}$$

with $\mu^{gas}_{N_2} = \mu^{\circ,gas}_{N_2}(T) + k_B T \ln(p_{N_2}/p^\circ)$ and $\mu^{liquid}_{N} = \mu^{\circ,liquid}_{N}(T) + k_B T \ln x_N$. Here, $\mu^{\circ,gas}_{N_2}(T)$ is the standard chemical potential of ideal N_2 at the standard pressure of 1 bar, $\mu^{\circ,liquid}_{N}(T)$ is the standard chemical potential of dissolved atomic N in the dilute Ga. Solving for the atomic-N molar concentration yields Henry's law:

$$x_{N_2}(T, p_{N_2}) = \exp\left(\frac{\frac{1}{2}\mu^{\circ,gas}_{N_2} - \mu^{\circ,liquid}_{N}}{k_B T}\right)\left(\frac{p_{N_2}}{p^\circ}\right)^{\frac{1}{2}} = \exp\left(-\frac{\Delta G^{N}_{solv}}{k_B T}\right)\left(\frac{p_{N_2}}{p^\circ}\right)^{\frac{1}{2}} \tag{S15}$$

Using $\Delta G^{N}_{solv} \approx 0.85$ eV at 1000 K, at which $k_B T \approx 0.086$ eV, gives the prefactor $\exp[-\Delta G^{N}_{solv}/k_B T] \approx 5 \times 10^{-5}$; thus $x_N \propto \sqrt{p_{N_2}}$ is extremely small even near 1 bar. Davydov *et al.*[12,13] and Unland *et al.*[14] evaluated the thermodynamic assessment of the Ga-N system[15–19] and gave empirical CALPHAD models. Fig. S6d compares the $x_N(T)$ curve from Eq. S15 with Davydov and Unland fit, as well as experimental data. The comparison is limited to 1400-1900 K, which is the temperature window analyzed in those models and covered by available measurements.

Supplementary Note S8: Crystallographic statistics of partially nitridated GaN/Ga particles

We indexed more than 200 partially nitridated GaN/Ga particles after 1 and 5 min N_2 plasma exposure. The crystallographic statistics are summarized in Fig. S7, and the identification of the crystal planes of individual GaN/Ga particles is presented in Fig. S8. Regardless of the nitridation time, the WZ polytype has roughly one third (67% at 1 min and 69% at 5 min), with the remainder of ZB.Within WZ, the most frequent orientations are the (0001) and $(11\bar{2}3)$, followed by prismatic/semipolar facets $(1\bar{1}00)$ and $(1\bar{1}01)$. Within ZB, (110) is predominant, and others facets, like (001), only have a small amount. The close agreement between the 1 and 5 min datasets indicates that polytype and facet selection are largely determined at nucleation, with subsequent nitridation primarily increasing particle size rather than altering crystallography.

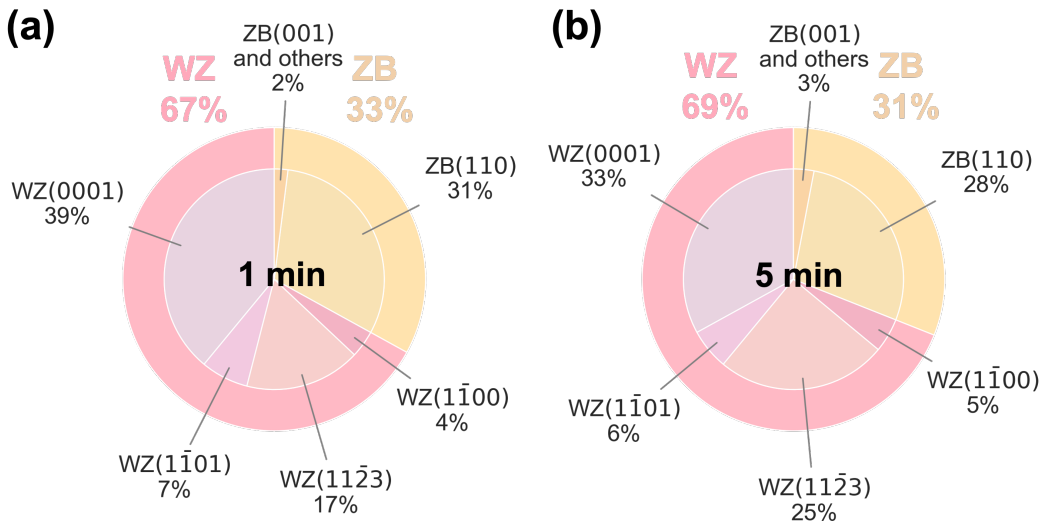

Figure S7. The crystallographic information and GaN radius of the 1 min and 5 min partially nitridated GaN/Ga particles. **(a)**-**(b)**: Distribution of crystal plane appearances in 1 min (**a**) and 5 min (**b**) partially nitridated GaN/Ga particles.

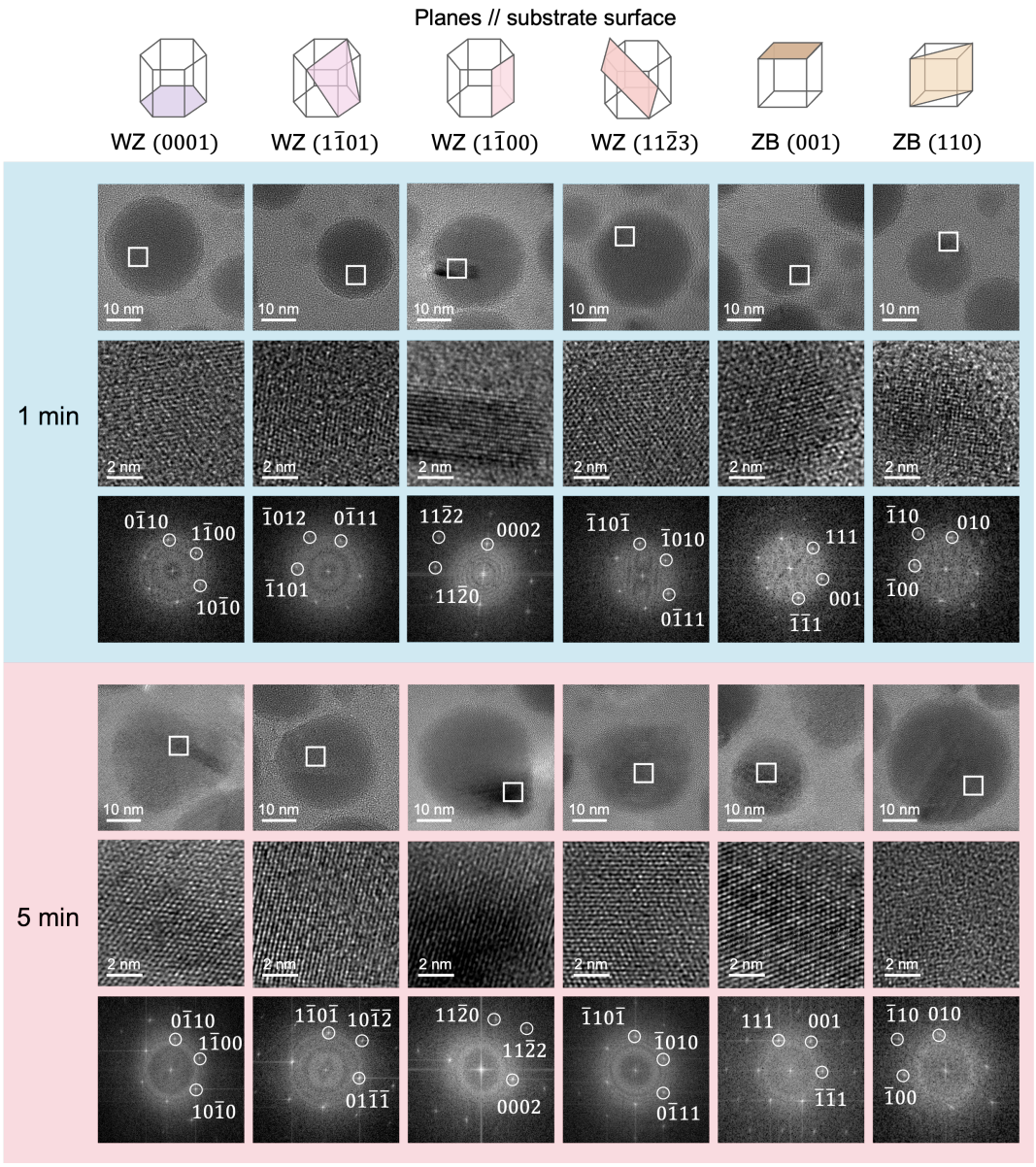

Figure S8. Identification of the crystal planes of individual GaN/Ga particles. Panels are grouped by nitridation time (top, blue: 1 min; bottom, pink: 5 min). For each crystallographic assignment, the top row shows a HAADF-STEM overview of a representative particle with a white square marking the region of interest; the middle row shows a HRTEM zoom of that boxed area; and the bottom row shows the 2D FFT of the HRTEM image with indexed reflections.

Supplementary Note S9: Interface-induced atomic ordering in the liquid phase in other III-nitride systems

The simulation setups for AlN(s)-Al(l) and InN(s)-In(l) interfaces follow the same setups as in the GaN(s)–Ga(l) system. In brief, we constructed WZ nitride slabs (8 layers, 768 atoms) exposing the polar basal planes, (0001) and $(000\bar{1})$, and placed them in contact with a liquid metal region of Al or In (500 atoms). The solid-melt interface cells were equilibrated using the same MD workflow (pressures/temperatures setups, thermostat/barostat settings and equilibration procedures) as described for GaN, and all profiles shown here are time-averaged over the equilibrated trajectories. Using the same analysis pipeline, we also computed the planar-averaged atomic number densities of the metal and N and the planar-averaged Bader charge distribution $q(z)$ along the interface-normal direction, enabling a direct comparison of interfacial layering and charge redistribution across GaN, AlN, and InN systems.

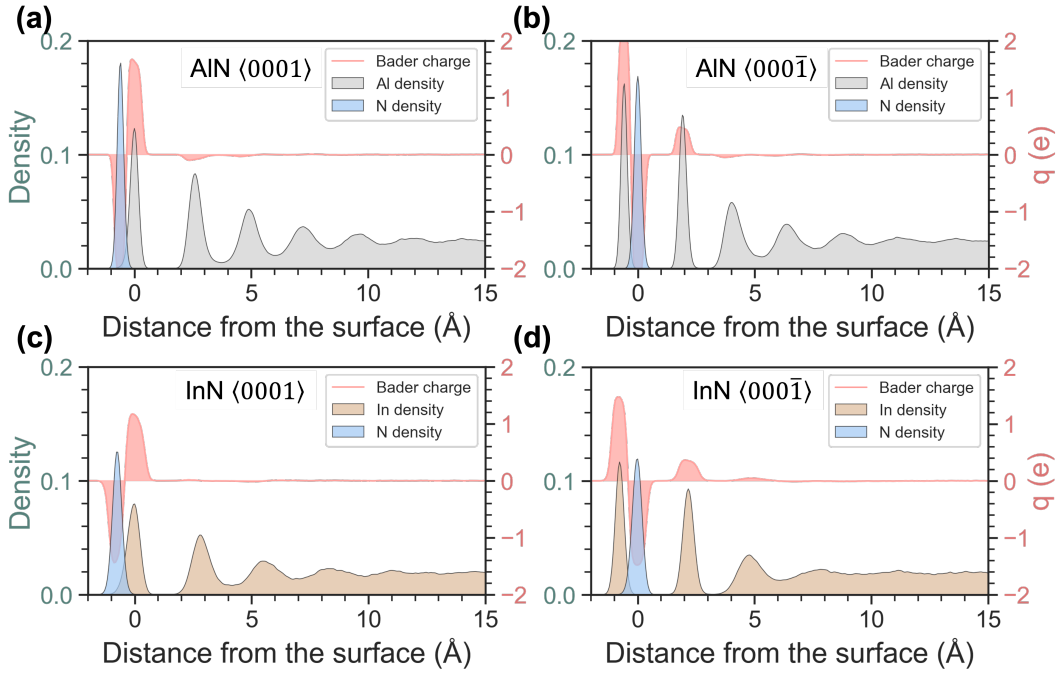

Figure S9. Atomic density and charge distribution at AlN(s)-Al(l) and InN(s)-In(l) interfaces. **(a)**: AlN Al-polar interface (0001). **(b)**: AlN N-polar interface (000$\bar{1}$). **(c)**: InN Al-polar interface (0001). **(d)**: InN N-polar interface (000$\bar{1}$). Left axis shows time-averaged atomic number density profiles along the surface-normal direction. The right axis shows the planar-averaged Bader charge $q(z)$ (red curves), plotted as a function of distance from the surface.

Both AlN(s)-Al(l) and InN(s)-In(l) interfaces exhibit pronounced metal layering next to the nitride, with a strong first metal density peak at the interface followed by damped oscillations that decay toward the bulk liquid for a few angstroms, indicating interface-induced ordering. In both cases, the planar-averaged Bader charge $q(z)$ is localized near the interface and oscillates with distance in a way that roughly follows the layering, then approaches near zero in the bulk liquid. Comparing materials, Al exhibits the sharpest peaks and the most persistent oscillations, whereas In shows broader peaks that damp out more quickly. In contrast, the Ga profiles in the GaN(s)-Ga(l results above display weaker and more rapidly decaying layering. A likely reason is the different reduced temperatures at 1000 K: Al is close to its melting point ($T/T_m \approx 1.07$), while In ($T/T_m \approx 2.33$) and especially Ga ($T/T_m \approx 3.30$) are much further above T_m. At the same absolute temperature, the higher T/T_m implies stronger thermal disorder and faster structural relaxation in the liquid, which tends to weaken interfacial layering and make the density oscillations decay more rapidly.

Supplementary References

1. Kresse, G. & Furthmüller, J. Efficiency of ab-initio total energy calculations for metals and semiconductors using a plane-wave basis set. *Comput. Mater. Sci.* **6**, 15–50, DOI: 10.1016/0927-0256(96)00008-0 (1996).
2. Kresse, G. & Furthmüller, J. Efficient iterative schemes for ab initio total-energy calculations using a plane-wave basis set. *Phys. Rev. B* **54**, 11169, DOI: 10.1103/PhysRevB.54.11169 (1996).
3. Perdew, J., Burke, K. & Ernzerhof, M. Generalized gradient approximation made simple. *Phys. Rev. Lett.* **77**, 3865–3868, DOI: 10.1103/PhysRevLett.77.3865 (1996).
4. Blochl, P. Projector augmented-wave method. *Phys. Rev. B* **50**, 17953–17979, DOI: 10.1103/PhysRevB.50.17953 (1994).
5. Henkelman, G., Uberuaga, B. P. & Jónsson, H. A climbing image nudged elastic band method for finding saddle points and minimum energy paths. *The J. Chem. Phys.* **113**, 9901–9904, DOI: 10.1063/1.1329672 (2000).
6. Henkelman, G. & Jónsson, H. Improved tangent estimate in the nudged elastic band method for finding minimum energy paths and saddle points. *The J. Chem. Phys.* **113**, 9978–9985, DOI: 10.1063/1.1323224 (2000).
7. Plimpton, S. Fast parallel algorithms for short-range molecular dynamics. *J. Comput. Phys.* **117**, 1–19, DOI: 10.1006/jcph.1995.1039 (1995).
8. Thompson, A. P. *et al.* LAMMPS - a flexible simulation tool for particle-based materials modeling at the atomic, meso, and continuum scales. *Comput. Phys. Commun.* **271**, 108171, DOI: 10.1016/j.cpc.2021.108171 (2022).
9. The PLUMED consortium. Promoting transparency and reproducibility in enhanced molecular simulations. *Nat. Methods* **16**, 670–673, DOI: 10.1038/s41592-019-0506-8 (2019-08).
10. Tribello, G. A., Bonomi, M., Branduardi, D., Camilloni, C. & Bussi, G. PLUMED 2: New feathers for an old bird. *Comput. Phys. Commun.* **185**, 604–613, DOI: 10.1016/j.cpc.2013.09.018 (2014).
11. Chugh, M. & Ranganathan, M. Adsorbate interactions on the GaN(0001) surface and their effect on diffusion barriers and growth morphology. *Phys. Chem. Chem. Phys.* **19**, 2111–2123, DOI: 10.1039/C6CP07254B (2017).
12. Davydov, A. V. & Anderson, T. J. Thermodynamic analysis of the Ga-N system. In *III-V Nitride Materials and Processes III*, 38–49 (1999).
13. Davydov, A., Boettinger, W., Kattner, U. & Anderson, T. Thermodynamic Assessment of the Gallium-Nitrogen System. *physica status solidi (a)* **188**, 407–410, DOI: 10.1002/1521-396X(200111)188:1<407::AID-PSSA407>3.0.CO;2-P (2001-11).
14. Unland, J., Onderka, B., Davydov, A. & Schmid-Fetzer, R. Thermodynamics and Phase Stability in the Ga–N System. *J. Cryst. Growth* **256**, 33–51, DOI: 10.1016/S0022-0248(03)01352-6 (2003-08).
15. Grzegory, I. *et al.* III–V nitrides—thermodynamics and crystal growth at high N2 pressure. *J. Phys. Chem. Solids* **56**, 639–647, DOI: 10.1016/0022-3697(94)00257-6 (1995).
16. Thurmond, C. D. & Logan, R. A. The equilibrium pressure of N2 over GaN. *J. Electrochem. Soc.* **119**, 622, DOI: 10.1149/1.2404274 (1972).
17. Logan, R. A. & Thurmond, C. D. Heteroepitaxial thermal gradient solution growth of GaN. *J. Electrochem. Soc.* **119**, 1727, DOI: 10.1149/1.2404088 (1972).
18. Madar, R., Jacob, G., Hallais, J. & Fruchart, R. High pressure solution growth of GaN. In Cullen, G. W., Kaldis, E., Parker, R. L. & Rooymans, C. J. M. (eds.) *Vapour Growth and Epitaxy*, 197–203, DOI: 10.1016/B978-1-4831-9854-5.50031-8 (Elsevier, 1975).
19. Karpiński, J., Jun, J. & Porowski, S. Equilibrium pressure of N2 over GaN and high pressure solution growth of GaN. *J. Cryst. Growth* **66**, 1–10, DOI: 10.1016/0022-0248(84)90070-8 (1984).